IAEA nuclear fusion

Edge turbulence transport during ELM suppression with *n* = 4 resonant magnetic perturbation on EAST

To cite this article: S.C. Liu *et al* 2023 *Nucl. Fusion* **63** 042003

OPEN ACCESS
IOP Publishing | International Atomic Energy Agency Nuclear Fusion
Nucl. Fusion 63 (2023) 042003 (13pp) https://doi.org/10.1088/1741-4326/acbce5

Edge turbulence transport during ELM suppression with $n = 4$ resonant magnetic perturbation on EAST

S.C. Liu[1,*], **Y. Liang**[1,2], **L.T. Li**[1,3], **T.F. Tang**[1,*], **X.H. Wu**[1,4], **N. Yan**[1], **T.H. Shi**[1], **G.S. Li**[1], **K.X. Ye**[1], **L.Y. Meng**[1], **R. Ding**[1], **Y. Sun**[1], **M. Jia**[1], **Q. Ma**[1,4], **Q. Zang**[1], **X. Li**[1], **S.X. Wang**[1], **M.R. Wang**[1,4], **H.L. Zhao**[1], **J.L. Wei**[1], **T. Zhang**[1], **Y.F. Jin**[1], **L. Liao**[1,4], **W.Y. Wei**[1,4], **Y. Li**[1,4], **R. Chen**[1], **G.H. Hu**[1], **N. Zhao**[5], **X.J. Liu**[1], **T.F. Ming**[1], **X. Han**[1], **W.B. Zhang**[1,4], **L. Wang**[1], **J.P. Qian**[1], **L. Zeng**[1], **G.Q. Li**[1], **G.S. Xu**[1], **X.Z. Gong**[1], **X. Gao**[1] **and the EAST Team**[a]

[1] Institute of Plasma Physics, Chinese Academy of Sciences, Hefei 230031, China
[2] Forschungszentrum Jülich GmbH, Institut für Energie- und Klimaforschung—Plasmaphysik, Partner of the Trilateral Euregio Cluster (TEC), 52425 Jülich, Germany
[3] Anhui University, 230039 Hefei, China
[4] University of Science and Technology of China, Hefei 230026, China
[5] School of Science, Southwest University of Science and Technology, Mianyang 621010, China

E-mail: shaocheng.liu@ipp.ac.cn and tang.tengfei.dut@gmail.com

Received 18 November 2022, revised 3 February 2023
Accepted for publication 17 February 2023
Published 6 March 2023

Abstract

The edge turbulence characteristics and the induced radial transport have been investigated in edge localized mode (ELM) suppression by using the $n = 4$ resonant magnetic perturbation coils on EAST, with $q_{95} = 3.6$ and the electron collisionality $\nu_e^* \approx 0.5$. During ELM suppression, the edge turbulence is enhanced dramatically, as measured by the reciprocating probe and the poloidal correlation reflectometry. In the near SOL, the low frequency turbulence (<30 kHz) has a large fluctuation level and propagates along the ion diamagnetic drift direction with a speed of 0.35 km s^{-1} in the plasma frame; an $n = 1$ electromagnetic mode around 120 kHz with a small k_θ ($\sim$0.15 cm^{-1}) appears when the ELM is suppressed; weak broadband turbulence between 40–120 kHz propagates in the electron diamagnetic drift direction with a velocity of 3.4 km s^{-1} in the plasma frame. During the ELM suppression, the radial turbulent particle flux, calculated in both the time and frequency domains, is much higher (can be up to five times) than that in the inter-ELM phase. Furthermore, the low frequency turbulence (<30 kHz) dominates the cross-field particle transport. The 120 kHz electromagnetic mode also contributes to outward particle flux, which is relatively small. A set of CGYRO simulations are performed to illustrate the nature of the 120 kHz electromagnetic mode and the low frequency turbulence, suggesting that the former is the micro-tearing mode and the latter is the ion temperature gradient mode. The bispectral analysis suggests a strong three-wave coupling between the low frequency and high frequency turbulence (>250 kHz), which could be beneficial to form the observed turbulent transport. The estimated upstream cross-field particle flux is consistent with

---

[a] See Wan *et al* 2017 (https://doi.org/10.1088/1741-4326/aa7861) for the EAST Team.
[*] Authors to whom any correspondence should be addressed.

1741-4326/23/042003+13$33.00 Printed in the UK

the total particle flux deposited on divertor targets, demonstrating that the enhanced radial turbulent particle transport is an important mechanism for particle exhaust in ELM suppression.

Keywords: resonant magnetic perturbation, ELM control, turbulence transport, EAST, tokamak

(Some figures may appear in colour only in the online journal)

---

1. Introduction

Edge localized mode (ELM), an magnetohydrodynamic (MHD) instability in the high-confinement mode (H-mode) plasma of tokamaks, could contribute to a large cross-field heat and particle transport, and lead to extremely high instantaneous heat flux at the divertor targets [1]. The divertor heat load caused by ELMs is a big challenge for the safety and lifetime of the first wall materials, especially in the large-size magnetic fusion devices with small power decay length at divertor plates. Therefore, the control of ELM and the accompanied heat load is a crucial issue in magnetically confined plasmas [2, 3]. Resonant magnetic perturbation (RMP) is one of the effective techniques to control ELMs, as demonstrated by the experiments in many tokamaks, such as DIII-D [4], JET [5, 6], ASDEX-Upgrade [7], MAST [8], EAST [9], KSTAR [10], and HL-2 A [11]. The cross-field transport during ELM mitigation or suppression is greatly enhanced, which helps maintain the heat and particle exhausts and facilitate the sustainment of ELM mitigation or suppression [12]. The understanding of radial transport caused by RMP is essential for the interpretation of ELM control. The RMP could increase the edge radial transport by creating a stochastic edge region through the overlap of the magnetic islands [13, 14], and the divertor particle patterns could be simulated by the field line tracing in the RMP experiment [15, 16]. Recently some simulation codes including the plasma response and plasma rotation during RMP application could provide more understandings on the MHD behaviors, turbulence and transport, such as MARS-Q and JOREK [17–19]. Turbulence plays an important role in radial transport during ELM control with RMP. In DIII-D tokamak, strong density pump-out is observed, and the low wavenumber density turbulence increases significantly over a wide radial region during ELM suppression by using $n = 3$ RMP [20]. During the ELM suppression with $n = 2$ RMP in DIII-D, the radial electric field decreases at the pedestal top, and the reduced $E \times B$ shear could enhance the drift-wave turbulence and the radial transport [21]. In ASDEX Upgrade, the low frequency broadband turbulence and a quasi-coherent mode can be observed during the ELM suppression phase, and both types of turbulence could contribute to the density pump-out and enhancement of radial transport [22]. During an ELM suppression experiment in KSTAR, the $E \times B$ flow decreases at the pedestal, and strong nonlinear coupling between turbulence eddies is observed [23]. In an ELM mitigation experiment with $n = 1$ RMP, an edge-coherent oscillation near 2 kHz in the steep-gradient pedestal region could provide continuous transport in HL-2 A [11]. In EAST, the broadband turbulence and the corresponding radial transport increase significantly in the plasma edge during ELM mitigation with $n = 1$ RMP [24]. In conclusion, the RMP has strong impacts on the edge turbulence characteristics and can affect the radial transport in the ELM control experiments.

ELM control has been systematically studied in EAST by using the up-down symmetric RMP coils, with eight upper coils and eight lower coils [9, 25, 26]. Recently, a series of ELM control experiments with $n = 4$ RMP in low q_{95} and low input torque plasma conditions have been performed in EAST, which is close to the ITER $Q = 10$ scenario [27, 28]. In this paper, the edge turbulence characteristics and the radial particle transport are investigated in the ELM suppression phase with $n = 4$ RMP. This paper is organized as follows. The experimental setup is described in section 2. The edge turbulence characteristics are presented in section 3. The edge turbulence transport is analyzed in section 4. A brief discussion is given in section 5. Section 6 is the conclusion.

2. Experimental setup

EAST is a superconducting tokamak with flexible divertor configurations, major radius $R_0 \leqslant 1.9$ m, minor radius $a \leqslant 0.45$ m [29]. In this experiment, the upper divertor is equipped with an ITER-like active water-cooling tungsten divertor target, and it is capable of handling a power load of up to 10 MW m^{-2} for a long-pulse steady-state plasma operation [30]. Several diagnostics are used to measure the edge plasma parameters and turbulence variations. A combined probe head mounted on the reciprocating probe (RCP) system at the outer midplane has been developed to study the edge turbulence structure and transport [31]. The sketch of the combined probe is shown in figure 1. The combined probe consists of two groups of the four-tip triple Langmuir probes (ϕ_{f1}, I_{s1}, ϕ_{+1} and ϕ_{f2}; ϕ_{f2}, I_{s2}, ϕ_{+2} and ϕ_{f3}) measuring the electron density and temperature, a Mach probe (I_{Mach1} and I_{Mach2}) measuring the parallel flow velocity, and two floating potential pins (ϕ_{f4} and ϕ_{f5}) at an inner plateau. The two pins of the double-probe (I_{s1} and ϕ_{+1}; I_{s2} and ϕ_{+2}) are connected through a biasing voltage of 190 V. The turbulence poloidal structure can be derived from the correlation of two floating potential signals among the pins (ϕ_{f1}, ϕ_{f2} and ϕ_{f3}; or ϕ_{f4} and ϕ_{f5}). The radial structure is calculated by pins ϕ_{f3} and ϕ_{f4}. All the Langmuir pins have a diameter of 2.5 mm and a length of 3 mm. Note that the poloidal distance between two adjacent pins is large enough to avoid the blocking effect of magnetic field line. The sampling rate of the RCP system is 1 MHz. With this probe arrangement,

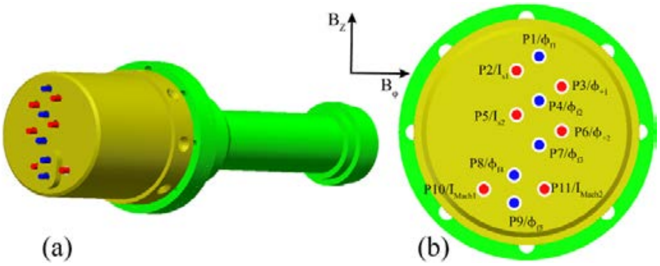

Figure 1. Sketch of the combined probe. (*a*) Side view; (*b*) front view. The blue pins measure the floating potential, and the red pins (P2, P3, P5 and P6) compose the double-probe. A Mach probe is composed of two red pins (P10 and P11). The physical name of each pin is labeled in panel (*b*). The directions of B_φ and B_Z are annotated for panel (*b*).

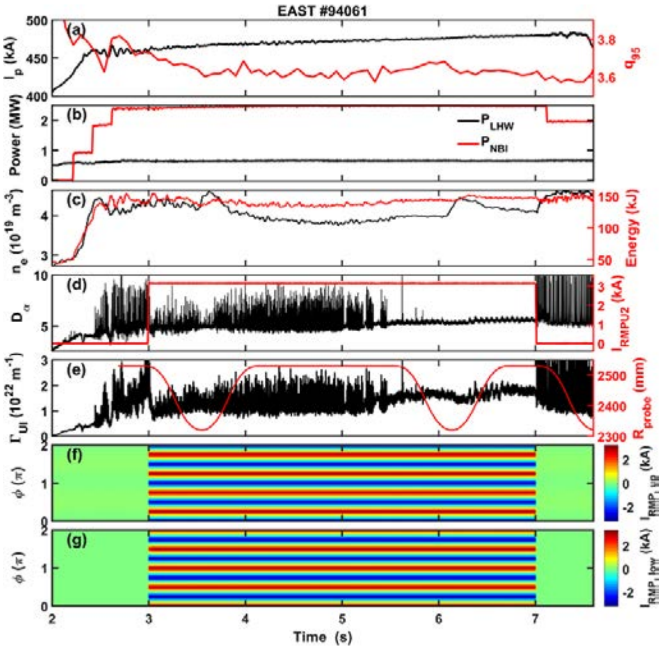

Figure 2. Temporal evolution of plasma parameter for discharge 94061 in EAST. (*a*) Plasma current and safety factor q_{95}; (*b*) LHW and NBI heating power; (*c*) plasma line averaged density and plasma stored energy; (*d*) D_α signal in the upper divertor and the current of an upper RMP coil; (*e*) divertor particle flux in the upper inner divertor and the radial position of RCP; (*f*) and (*g*) are the currents of the upper and lower RMP coils, respectively.

the radial heat and particle transport and the Reynold stress can be measured at the same time.

The divertor Langmuir probe (DivLP) system on EAST has been operated successfully since 2007 and has become a key diagnostic for the study of divertor physics [32]. In the upper divertor, two toroidal arrays of DivLPs are located at ports D and O, with a poloidal resolution from 12 to 18 mm [33]. In the lower divertor, the DivLP array is at port D with a resolution of 15 mm and 10 mm for the lower inner (LI) and lower outer (LO) targets, respectively. The sampling rate of the DivLP system is 50 kHz. An ordinary-mode multi-channel poloidal correlation reflectometry (PCR), located at the outer midplane of port K, has been developed in EAST to measure the density fluctuations from the scrape-off layer (SOL) to the pedestal [34]. The profile of electron density is measured by a polarimeter-interferometer (POINT) system [35] and density profile reflectometer [36]. The profile of electron temperature is measured by the Thomson scattering (TS) system [37].

3. Characteristics of edge turbulence

3.1. Characteristics of global plasma parameters

The edge turbulence characteristics and the induced radial transport have been investigated in a series of ELM control experiments with $n = 4$ RMP in EAST. Typical plasma parameters are listed in figure 2. The plasma current I_p increases from 450 kA to 480 kA; meanwhile, the safety factor q_{95} at the 95% normalized poloidal flux surface decreases from 3.8 to 3.58. Some key plasma parameters are as follows: the neutral beam injection (NBI) heating power $P_\mathrm{NBI} = 2.5$ MW, the low hybrid wave (LHW) heating power $P_\mathrm{LHW} = 0.65$ MW, line-averaged density $n_\mathrm{e} = 3.8\text{–}4.5 \times 10^{19}\ \mathrm{m}^{-3}$, plasma stored energy 145 kJ, $\beta_\mathrm{N} = 1.5$, toroidal field $B_\mathrm{T} = 1.7$ T in the clockwise direction viewed from the top, and an upper single null divertor configuration ($\mathrm{d}R_\mathrm{sep} = 35$ mm). The toroidal mode number is $n = 4$ for the upper and the lower RMPs, with a maximum coil current of 3 kA and a phase difference $\delta\phi_\mathrm{UL} = \phi_\mathrm{U} - \phi_\mathrm{L} = 180°$ between the upper and the lower RMP coils. As illustrated in figure 2(*d*), when the RMP coil is turned on, the big ELM is mitigated greatly after $t = 3$ s, with the relative fluctuation amplitude $\delta I_{D_\alpha}/I_{D_\alpha}$ decreasing from 0.5 to 0.2. When the q_{95} decreases gradually with the increase of plasma current, an ELM suppression is achieved from $t = 5.46$ s. Before this ELM suppression, there are three short time periods ($t \sim 5.02$ s, 5.22 s, 5.32 s) with ELM suppression, indicating marginal plasma conditions for ELM suppression. After the RMP coil is turned off at $t = 7$ s, the big ELMs reappear immediately. A strong density pump-out effect is observed during the ELM suppression phase, corresponding to $n_\mathrm{e} = 4.6 \times 10^{19}\ \mathrm{m}^{-3}$ and $4.1 \times 10^{19}\ \mathrm{m}^{-3}$ for the ELMy phase and ELM suppression phase, respectively. However, the plasma stored energy remains constant at 145 kJ in this period, indicating good plasma confinement in the ELM suppression phase. The particle flux deposited on the upper inner (UI) divertor target is presented in figure 2(*e*). The baseline of Γ_UI in the ELM suppression phase is much higher than that in the ELMy phase, which is consistent with the temporal variation of D_α signal in figure 2(*d*), denoting significant enhancement of outward particle flux in the ELM suppression. The RCP is plunged three times in this discharge to measure the edge turbulence behaviors, as shown in the red curve of figure 2(*e*).

The fitted electron temperature and electron density in ELM suppression and ELMy phase are shown in figure 3. Note that the electron temperature is fitted according to the TS data. The electron density is fitted according to the measurements of POINT and density profile reflectometer. In the core plasma, the electron density in the ELMy phase is much higher

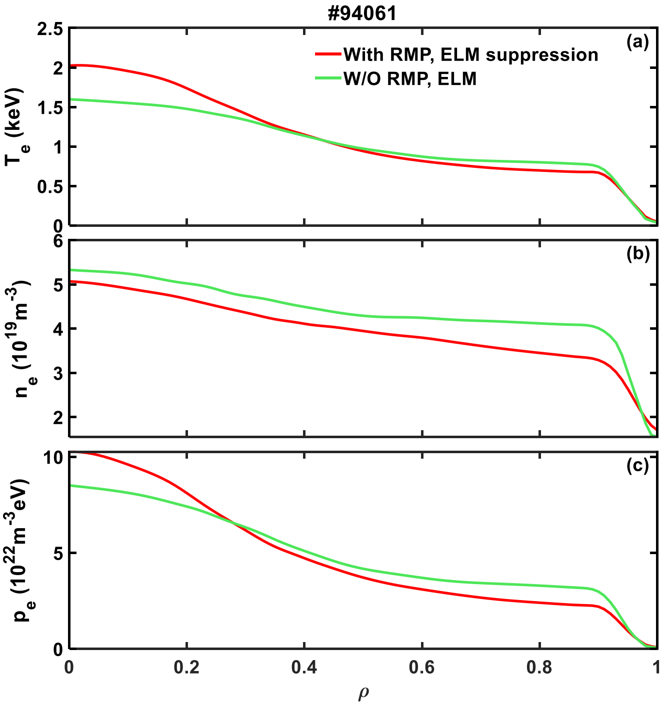

Figure 3. The fitted electron temperature (a), electron density (b) and electron pressure (c) for discharge 94061. The horizontal axis ρ is the square root of the normalized toroidal flux.

than that in the ELM suppression phase, which is consistent with the density pump-out effect in the line averaged density; while the electron temperature only has a slight change in the radial region of $0.3 \leqslant \rho \leqslant 0.9$, and therefore the electron pressure in this region is a bit lower in the ELM suppression case. In the edge plasma close to the last closed flux surface (LCFS), the electron density in ELM suppression is about 10% higher than that in the ELMy phase. Besides, the ELM suppression case has a much lower pedestal height but larger SOL density, signifying enhancement of particle exhaust when ELM is suppressed by the $n = 4$ RMP. At the pedestal top the electron temperature and density are $T_{\mathrm{e}} \approx 700$ eV and $n_{\mathrm{e}} \approx 3.3 \times 10^{19}$ m^{-3}, hence the electron collisionality $\nu_{\mathrm{e}}^{*} \approx 0.5$ can be obtained from the equation $\nu_{\mathrm{e}}^{*} = 6.921 \times 10^{-18} Rqn_{\mathrm{e}}Z_{\mathrm{eff}}\ln\Lambda_{\mathrm{e}}/\left(\varepsilon^{3/2}T_{\mathrm{e}}^{2}\right)$, where R is the major radius in meter, q is the safety factor at the pedestal top, $\varepsilon = r/R_0$ is the inverse aspect ratio, $Z_{\mathrm{eff}} = 1.2$ is the effective ion charge, $\ln\Lambda_{\mathrm{e}} = 31.3 - \ln\left(\sqrt{n_{\mathrm{e}}}/T_{\mathrm{e}}\right)$ is the Coulomb logarithm, n_{e} is in m^{-3} and T_{e} is in eV [38]. The pedestal top is located at $\rho = 0.91$ ($R = 2.263$ m).

The divertor profiles of electron density and temperature for the ELMs and ELM suppression cases are illustrated in figure 4, with the locations of DivLPs mapped to the outer midplane. The electron temperature peaks near the LCFS and decreases gradually in the SOL. The electron density also peaks around the LCFS, but has a flat distribution in the SOL with considerable value. Compared with the ELM case without RMP, the ELM suppression case with RMP has a larger electron temperature around the LCFS, but has a similar electron density distribution in the SOL. From these measurements, slight increases of the electron temperature and the corresponding particle flux are observed in the ELM suppression. Note that the 3D distribution of heat and particle fluxes during the application of RMP could reveal strong toroidal asymmetry [15], therefore the divertor conditions could be different toroidally.

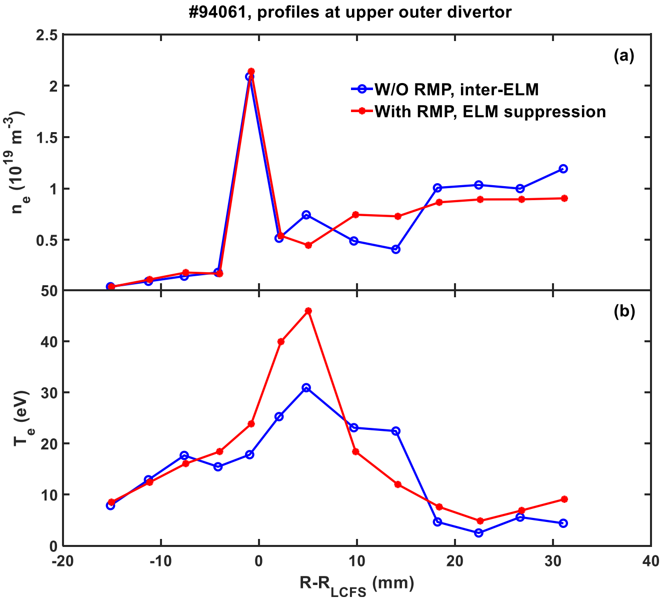

Figure 4. Divertor profiles of electron density (a) and temperature (b) for the ELMs and ELM suppression cases. The radial locations of DivLPs are mapped to the outer midplane.

3.2. Characteristics of edge turbulence

Figure 5 shows the temporal evolution of the auto-correlation power spectral density (APSD) for the core PCR (near the pedestal top, $\rho = 0.94$), edge PCR (near the LCFS, $\rho = 1.03$), Mirnov coil embedded in the vacuum chamber and the floating potential measured by the RCP [39]. From the APSD of the PCR at the pedestal top, the power intensity below 200 kHz is larger in ELM suppression than that in ELM mitigation and natural ELMy phase, but the fluctuation level in the high frequency range (above 200 kHz) is much lower in the ELM suppression case. Note that the decrease of APSD around $t = 6.1$ s in figure 5(b) is caused by the sharp increase of line averaged electron density that changes the position of PCR measurement, as illustrated in figure 2(c). For the PCR channel near the LCFS, the density fluctuation level in ELM suppression is enhanced significantly in the frequency range below 200 kHz compared with the ELM mitigation and the natural ELM phase, which is similar to the PCR channel at the pedestal top. As shown in figure 5(d), the APSD of the Mirnov coil in the ELMy phase without RMP exhibits a magnetic coherence mode around 20 kHz and a high-frequency mode (HFM) about 190 kHz. Note that both modes are usually observed in the H-mode plasma of EAST, and they have been investigated in previous publications [40–42]. In the ELM suppression phase, the APSD of the magnetic coil is much larger than the other

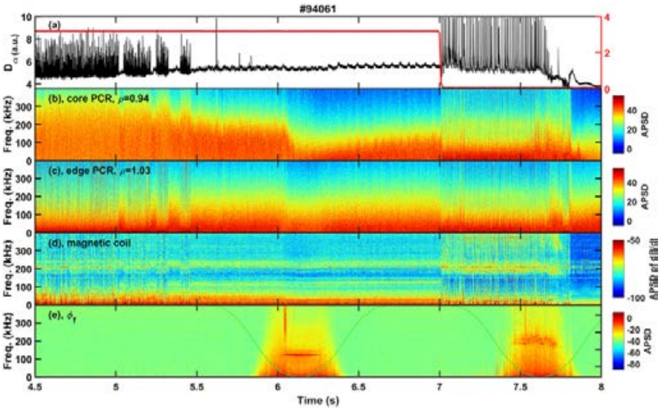

Figure 5. (*a*) D_α signal at the upper divertor and the current of an upper RMP coil; the APSD of core PCR (*b*), edge PCR (*c*), magnetic coil (*d*), floating potential measured by the RCP and its radial position (blue curve) (*e*). The radial position of the PCR signal is annotated in (*b*) and (*c*).

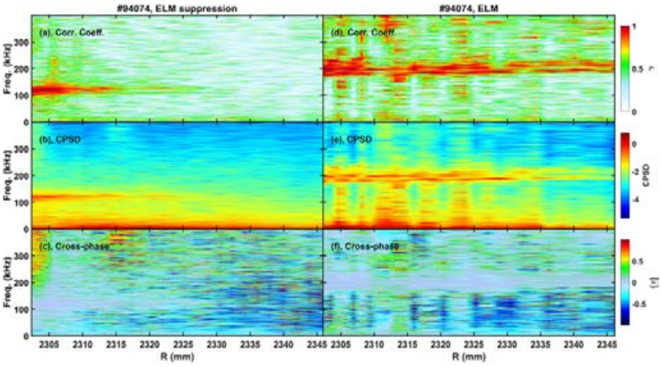

Figure 6. Radial distribution of the cross-correlation between two floating potential signals. The left panels are for the ELM suppression phase with RMP, and the right panels are for the ELMy phase without RMP. (*a*) and (*d*): cross-correlation coefficient; (*b*) and (*e*): CPSD; (*c*) and (*f*): cross-phase.

two cases, especially in the frequency region below 30 kHz. It is obvious that a coherent mode located at 27 kHz appears in the ELM suppression phase. There is a magnetic mode about 5 kHz in the ELM suppression phase, i.e. its APSD is strong at the beginning but becomes weak gradually. Besides, another coherent magnetic mode between 115 kHz and 128 kHz is only observed when ELM is suppressed, which also can be found in the three short time periods ($t \sim 5.02$ s, 5.22 s, 5.32 s) of ELM suppression. As derived from the Mirnov coil system, this mode has a toroidal mode number of $n = 1$ and a poloidal mode number $m \approx 3$–4, and it propagates along the co-current direction (anti-clockwise viewed from the top). In figure 5(*e*), when the combined probe is plunged deep enough, a strong coherent mode centered at 123 kHz appears in ELM suppression but is absent in the ELMy phase. To summarize, the background turbulence below 200 kHz is enhanced significantly in the ELM suppression phase, especially below 30 kHz in the magnetic fluctuations; an electromagnetic mode around 120 kHz with $n =$ 1 is observed only in the ELM suppression.

In order to obtain the radial structure of edge turbulence, the cross-correlation between two poloidal separated floating potential signals is shown in figure 6. Note that discharge 94074 has the same plasma conditions as that of 94061, but the former discharge has a much deeper RCP plunge. Consequently, the combined probe data of discharge 94074 is used to analyze the SOL turbulence structure. From the cross-correlation coefficient and the cross-correlation power spectral density (CPSD) in figures 6(*a*) and (*b*), the electromagnetic mode around 120 kHz can be observed from $R = 2330$ mm in the ELM suppression, and becomes more pronounced with the decreasing R. Since the LCFS is located at $R_{\mathrm{LCFS}} = 2285$ mm, this mode can be detected in a wide SOL region (45 mm far away from LCFS). The cross-correlation coefficient of this mode is very high (close to 1) in the near SOL, while the cross-phase is very small in figure 6(*c*). In the ELMy phase without RMP, the SOL turbulence between two adjacent ELMs is weak, except for the prominent existence of the HFM.

The APSD of floating potential and ion saturation current in three radial positions is compared between the ELMy phase without RMP and the ELM suppression phase with RMP, as presented in figure 7. Note that the APSD in the ELMy case is calculated during the interval of two adjacent ELMs. The APSD is fitted by the spectral power decay function $S \propto f^{\alpha}$, where S is the APSD, and the decay factor α is annotated in each panel. In contrast with the no RMP case, the APSD among 1–100 kHz in ELM suppression is much higher at all the three radial positions in figure 7. This discrepancy is extremely remarkable in the low frequency range below 30 kHz. The electromagnetic mode around 120 kHz in ELM suppression can be seen in $R =$ 2317–2327 mm, and gets stronger in $R =$ 2307–2317 mm. Besides, two weak modes near 5 kHz and 27 kHz can be detected when the probe is close to the LCFS, as shown in figures 7(*b*) and (*c*). In the near SOL, the decay factor is $\alpha \approx -1.5$ for the ELM suppression case, and $\alpha = -1.2$ for the ELMy case. In the ASPD of ion saturation current in figures 7(*d*)–(*f*), the low frequency turbulence below 40 kHz is enhanced significantly in the ELM suppression, and the broadband turbulence between 40–120 kHz also increases. However, the 120 kHz mode is not obvious in the ASPD of the ion saturation current. The high frequency turbulence between 300–400 kHz raises dramatically in the near SOL for the ASPD of ion saturation current, which is much weaker in the APSD of floating potential, as shown in figures 7(*f*) and (*c*). In addition, the HFM around 190 kHz in the ELMy phase exhibits a large peak in the ASPD of ϕ_f and I_s, which is different from the 120 kHz mode in ELM suppression.

To gain the statistical properties of the SOL turbulence, the poloidal wavenumber-frequency power spectral density $S(k_\theta,f)$ and the conditional spectrum $S(k_\theta|f) = S(k_\theta,f)/S(f) = S(k_\theta,f)/\sum_{k_\theta} S(k_\theta,f)$ are derived by the two-point cross-correlation technique [43, 44], as shown in figures 8 and 9, respectively. From the spectrum $S(k_\theta,f)$ of ELMy phase in figure 8, the HFM around 190 kHz is prominent in the whole SOL with $k_\theta \approx 0.3$ cm^{-1} on the side of electron diamagnetic drift. In the low frequency region (below

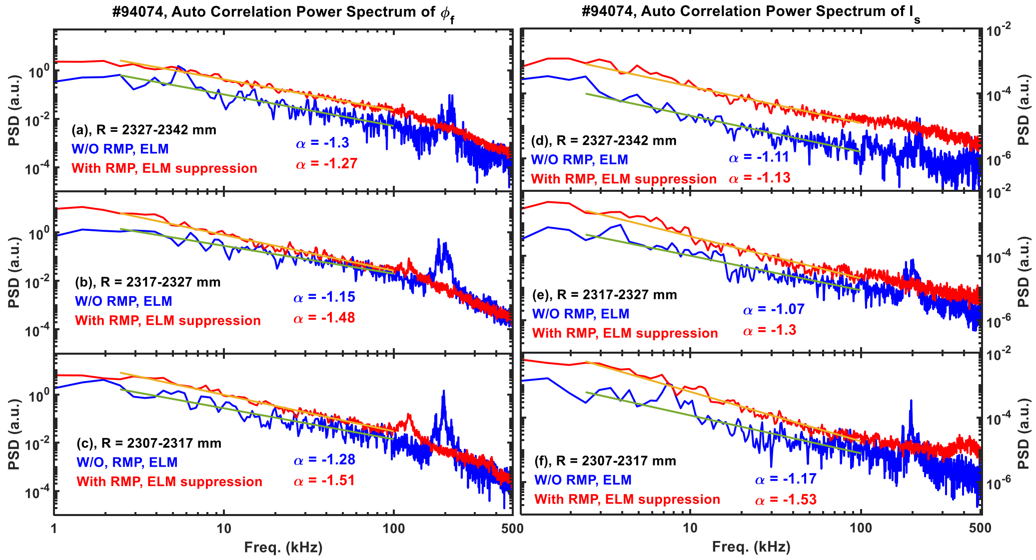

Figure 7. APSD of floating potential measured by the combined probe in three radial positions, as annotated in panels (*a*)–(*c*). The APSD of ion saturation current is shown in (*d*)–(*f*). The blue curve denotes the ELMy phase without RMP, and the red curve denotes the ELM suppression phase with RMP. The power decay factor α fitted in 2–100 kHz is given in each panel.

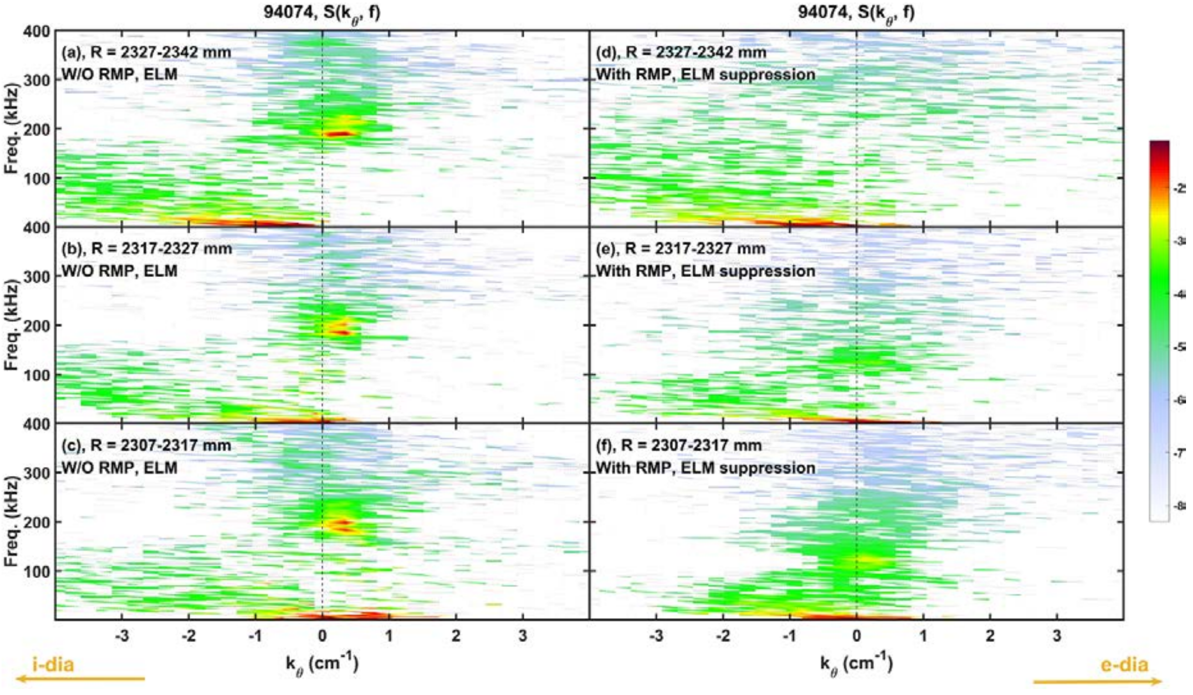

Figure 8. The poloidal wavenumber-frequency power spectral density $S(k_\theta,f)$ for the ELMy phase (left panels) and the ELM suppression phase (right panels). The probe radial position is labeled in each panel. The negative k_θ denotes the direction of ion diamagnetic drift.

20 kHz), the spectrum $S(k_\theta,f)$ also has large intensity. From the far SOL to the near SOL, the k_θ of fluctuations below 10 kHz moves from the negative side to the positive side, i.e. from the ion diamagnetic drift (ω_{*i}) direction to the electron diamagnetic drift (ω_{*e}) direction. In the frequency region below 150 kHz, there is a clear turbulence structure distributed in the ω_{*i} direction. However, the fluctuation level below 190 kHz between two adjacent ELMs is much lower than that in the ELM suppression phase, as shown in figures 5 and 7. It should be pointed out that the contribution of ELM eruption is taken into account in the calculation of $S(k_\theta,f)$ in figures 8(*a*)–(*c*), which could enhance the intensity of $S(k_\theta,f)$ in the frequency space. For the ELM suppression phase in figures 8(*d*)–(*f*), most of the poloidal cross-power $S(k_\theta,f)$ is concentrated in the low frequency region (<30 kHz). The electromagnetic mode around 120 kHz appears in figure 8(*e*) and becomes more prominent in figure 8(*f*). The poloidal wave number of this mode is centered at $k_\theta = 0.15\ \mathrm{cm}^{-1}$ in the near SOL, and the parameter $k_\theta\rho_\mathrm{s} \approx 0.01$ with an ion sound Larmor radius $\rho_\mathrm{s} = 0.7$ mm. With the increase of ρ_s in the pedestal,

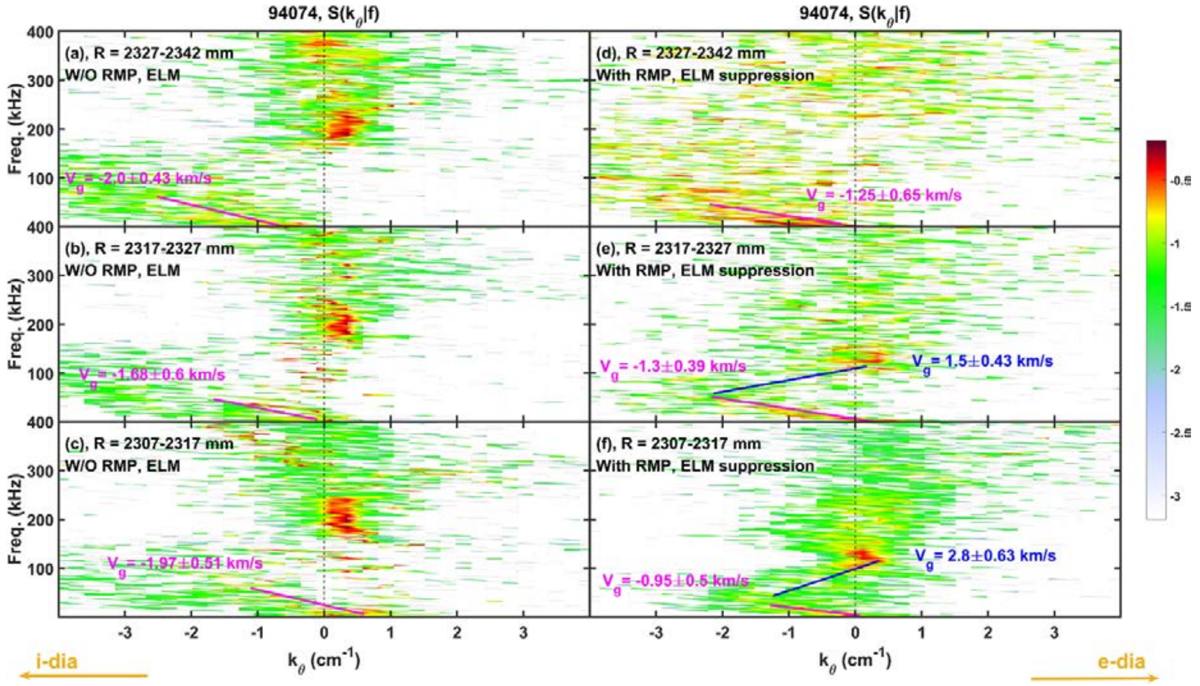

Figure 9. The conditional poloidal wavenumber-frequency power spectral density $S(k_\theta|f)$ for the ELMy phase (left panels) and the ELM suppression phase (right panels). The group velocity of the turbulence in a certain frequency region is fitted and annotated in each panel.

the parameter $k_\theta\rho_\mathrm{s}$ of this 120 kHz mode could reach 0.035, and the corresponding electron diamagnetic drift frequency is about $\omega_{*e} = -k_\theta T_\mathrm{e}/(eBP_\mathrm{e})\,\mathrm{d}P_\mathrm{e}/\mathrm{d}r \approx 80$ kHz in the pedestal. For the low frequency turbulence in ELM suppression, the k_θ is from 0 to -1.5 cm^{-1}, and the corresponding parameter $k_\theta\rho_\mathrm{s}$ is about 0.1 in the near SOL and up to 0.35 in the pedestal.

The group velocity of turbulence estimated from the slope $V_\mathrm{group} = 2\pi\Delta f/\Delta k_\theta$ is shown in figure 9. This group velocity is calculated by fitting k_center and $f(k_\mathrm{center})$ with a linear function $f = ak_\mathrm{center} + b$ within the frequency range of a turbulence structure, i.e. 0–30 kHz for the low frequency turbulence and 40–120 kHz for the broadband turbulence in figure 9(*f*). Here $k_\mathrm{center}(f_i) = \left[\sum_{k_\theta} k_\theta S_{f(i)}(k_\theta|f)\right] / \sum_{k_\theta} S_{f(i)}(k_\theta|f)$ is the barycenter of $S(k_\theta|f)$ at the frequency slice f_i, where $S_{f(i)}(k_\theta|f)$ is the conditional CPSD at frequency f_i. The error bar of the group velocity is given by fitting. In the ELMy phase, the group velocity of the turbulence below 100 kHz is about 1.68–2 km s^{-1} along the ion diamagnetic drift direction in the whole SOL, indicating the same fluctuation property that is probably related to the ELMs. In the ELM suppression phase, the low frequency turbulence (<30 kHz) has a group velocity of about 1.25 km s^{-1} (along the ω_{*i} direction) in the far SOL and 0.95 km s^{-1} in the near SOL; while the broadband turbulence between 40 kHz and 120 kHz in the near SOL has a group velocity of about $V_\mathrm{g} = 2.8$ km s^{-1} along the ω_{*e} direction. As derived from the probe data, the poloidal electric drift velocity $V_{E\times B} = E_r/B_\varphi$ is about 0.6 km s^{-1} along the ω_{*i} direction. In the near SOL, the turbulence propagation velocity in the plasma frame could be estimated by $V_\mathrm{plasma} = V_\mathrm{lab} - V_{E\times B}$, i.e. about 0.35 km s^{-1} along the ω_{*i} direction for the low frequency turbulence and 3.4 km s^{-1} along the ω_{*e} direction for the broadband turbulence in figure 9(*f*).

The poloidal statistical parameters are derived from the two-point cross-correlation analysis within the 1–400 kHz frequency range, as illustrated in figure 10. For the ELMy case without RMP, the variations of the statistical parameters are small in the whole SOL, though the averaged poloidal wave number $\langle k_\theta\rangle = \sum_f \bar{k}_\theta(f)S(f)$ and the correlation coefficient $\gamma = \langle\sum_f[\gamma(f).P_{xy}(f)]/\sum_f P_{xy}(f)\rangle$ increase gradually with the decreasing R, where $P_{xy}(f)$ and $\gamma(f)$ are the CPSD and cross-coefficient from cross-correlation calculation, respectively, and the angle bracket here denotes the ensemble average. For the ELM suppression case, the statistical parameters have large radial variations. In figure 10(*d*), the averaged frequency $\langle f\rangle = \sum fS(f)$ increases significantly from 20 kHz to 70 kHz when $R <$ 2320 mm, where the intensity of the electromagnetic mode around 120 kHz also rises greatly, as illustrated in figures 6 and 7. It is suggested that this electromagnetic mode and the broadband turbulence within 40–120 kHz have an important contribution to the statistical parameters. From the far SOL to the near SOL, $\langle k_\theta\rangle$ changes gradually from -1.2 cm^{-1} to -0.1 cm^{-1} (in ω_{*i} direction), γ increases from 0.45 to 0.8, the poloidal correlation length $l_{c_\theta} = 1/\langle\sigma_{k\theta}\rangle = 1/\sqrt{\langle\sigma^2_{k\theta}\rangle}$ increases from 0.7 cm to 2.3 cm, the turbulence poloidal phase velocity defined by $V_\mathrm{phase} = \sum_{k_\theta,f} 2\pi fS(k_\theta,f)/k_\theta$ is very small when $R >$ 2320 mm but increases sharply in the near SOL. The poloidal wave number spectral width is given by $\langle\sigma^2_{k_\theta}\rangle = \sum_f \bar{\sigma}^2_{k_\theta} S(f) = \sum_f S(f)\left\{\sum_{k_\theta}\left[k_\theta - \bar{k}_\theta(f)\right]^2 S(k_\theta|f)\right\}$.

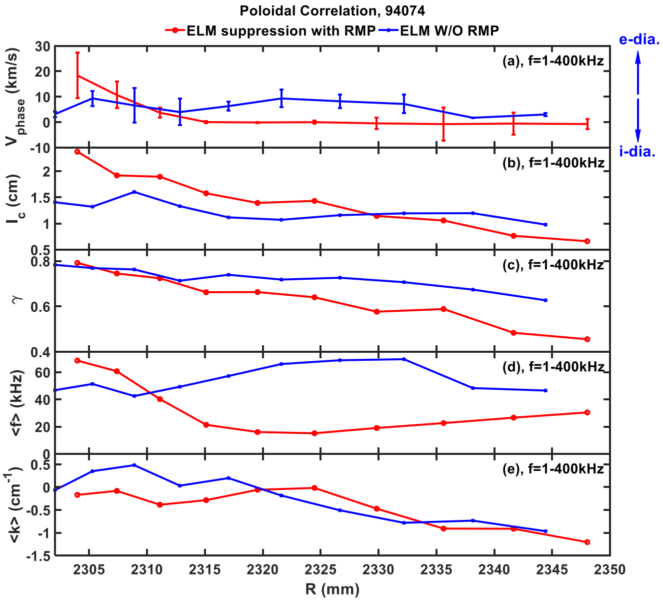

Figure 10. The poloidal statistical parameters for the ELM suppression phase (red curve) and the ELMy phase (blue curve), with a frequency range of 1–400 kHz used in the calculation. (*a*) Turbulence poloidal phase velocity, and the error bar denoting the standard deviation; (*b*) poloidal correlation length; (*c*) correlation coefficient; (*d*) averaged frequency; (*e*) averaged poloidal wave number. The positive poloidal phase velocity is in the electron diamagnetic drift direction, while the negative phase velocity is in the ion diamagnetic drift direction.

To summarize, the electromagnetic mode at 120 kHz and the broadband turbulence in ELM suppression reveal high turbulence phase velocity V_{ph} and poloidal correlation length l_{c}, but low poloidal wave number $\langle k_\theta \rangle$. It should be noted that the low frequency turbulence (<30 kHz) in ELM suppression has a much larger fluctuation level than the broadband turbulence and the electromagnetic mode at 120 kHz, as shown in figures 5, 7 and 8. In addition, the electromagnetic mode exhibits strong fluctuations in the floating potential but much weaker in the ion saturation current. Note that the geodesic acoustic mode (GAM) frequency at the pedestal is $f_{\mathrm{GAM}} = \sqrt{[(T_{\mathrm{i}}+T_{\mathrm{e}})/m_{\mathrm{i}}].[7/4+T_{\mathrm{e}}/T_{\mathrm{i}}]}/2\pi R \approx 28$ kHz, which is close to the coherent mode at 27 kHz in figures 5 and 7.

4. Edge turbulence transport

The radial particle flux driven by turbulence can be derived in the time and frequency domains from the fluctuations of electron density, temperature, and the poloidal electric field. The time domain turbulent particle and heat fluxes are calculated by the following formulas:

$$\Gamma_{\mathrm{e}} = \langle \tilde{n}_{\mathrm{e}} \tilde{V}_{\mathrm{r}} \rangle = \frac{\langle \tilde{n}_{\mathrm{e}} \tilde{E}_\theta \rangle}{B_\varphi}, \quad (1)$$

$$Q_{\mathrm{e}} = \frac{3}{2} \langle \tilde{P}_{\mathrm{e}} \tilde{V}_{\mathrm{r}} \rangle = \frac{3T_{\mathrm{e}} \langle \tilde{n}_{\mathrm{e}} \tilde{E}_\theta \rangle}{2B_\varphi} + \frac{3n_{\mathrm{e}} \langle \tilde{T}_{\mathrm{e}} \tilde{E}_\theta \rangle}{2B_\varphi}, \quad (2)$$

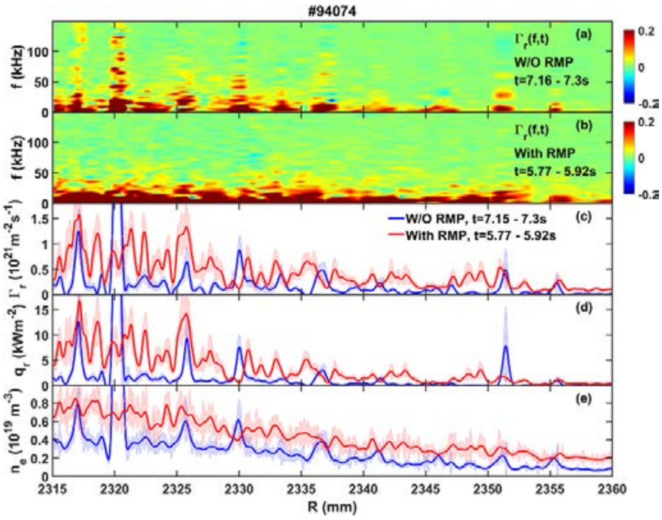

Figure 11. Radial turbulent particle flux in the frequency space for the ELMy phase (*a*) and ELM suppression phase (*b*) at the outer midplane; (*c*) radial turbulent particle flux; (*d*) radial turbulent heat flux; (*e*) SOL electron density. The positive Γ_r signifies the outward particle flux, while the negative value means the inward particle flux. The shaded regions in (*c*)–(*e*) denote the standard deviation of particle flux and electron density, respectively.

where the tilde on the top denotes the signal fluctuations, the angle bracket means the ensemble average, B_φ is the toroidal magnetic field, $V_{\mathrm{r}} = E_\theta / B_\varphi$, and $E_\theta = (\phi_{f2} - \phi_{f1})/d$. The particle flux in the frequency domain can be calculated from the CPSD between the fluctuations of electron density and electric field, as shown in the following formula:

$$\Gamma_e(f) = \frac{2\left\langle \left| P_{\tilde{n}_e \tilde{E}_\theta}(f) \right| \cos\left(\alpha_{\tilde{n}_e \tilde{E}_\theta}(f)\right) \right\rangle}{B_\varphi}, \quad (3)$$

where $P_{\tilde{n}_e \tilde{E}_\theta}(f)$ is the CPSD of $\tilde{n}_e$ and $\tilde{E}_\theta$, and $\alpha_{\tilde{n}_e \tilde{E}_\theta}(f)$ is the cross-phase angle.

The frequency distribution of radial turbulent particle flux at the outer midplane is shown in figures 11(*a*) and (*b*), corresponding to the ELMy phase without RMP and the ELM suppression phase with $n = 4$ RMP. In the ELMy phase, the transient particle flux caused by ELMs is extremely large and directed outwards, but the particle flux between two adjacent ELMs is very small. In the ELM suppression phase, most of the particle flux $\Gamma_{\mathrm{r}}(f,t)$ is concentrated in the low frequency range (<30 kHz) in a wide SOL, and this particle flux driven by the low frequency turbulence is enhanced in the near SOL. In addition, the electromagnetic mode around 120 kHz also contributes to outward particle flux in the near SOL, but its intensity is much lower than that of the low frequency turbulence. The radial turbulent particle flux calculated in the time domain is presented in figure 11(*c*). The particle flux during ELM suppression is several times larger than that in the inter-ELM phase through the whole SOL, and the ratio between them could be up to 5 in the near SOL. The radial particle diffusion coefficient can be estimated by $\Gamma_{\mathrm{e}} = -D_{\mathrm{e}} \partial n_{\mathrm{e}} / \partial r$, with $D_e \approx 2 - 3\,\mathrm{m}^2\mathrm{s}^{-1}$ in the near SOL for the ELM suppression phase. The turbulent heat flux

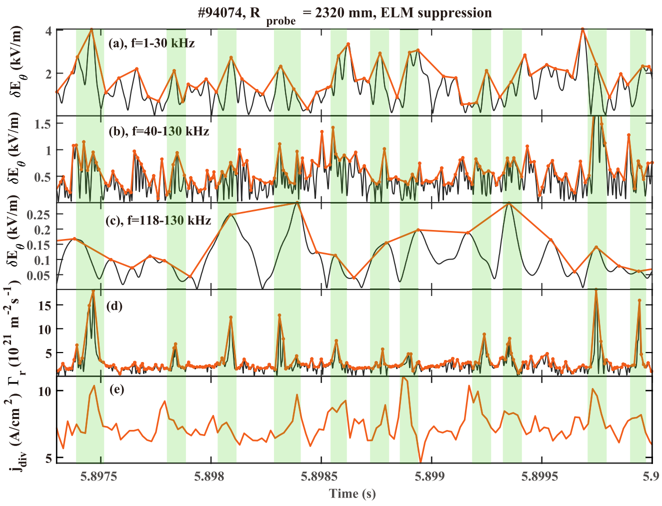

Figure 12. Envelope of fluctuations for the poloidal electric field in the frequency range of (*a*) 1–30 kHz, (*b*) 40–130 kHz, and (*c*) 118–130 kHz. (*d*) Envelope of the radial turbulence particle flux. (*e*) Ion saturation current density of a DivLP channel near the strike point, with its time sequence shifted by 530 μs backwards. The shaded strips denote the same event of particle exhaust.

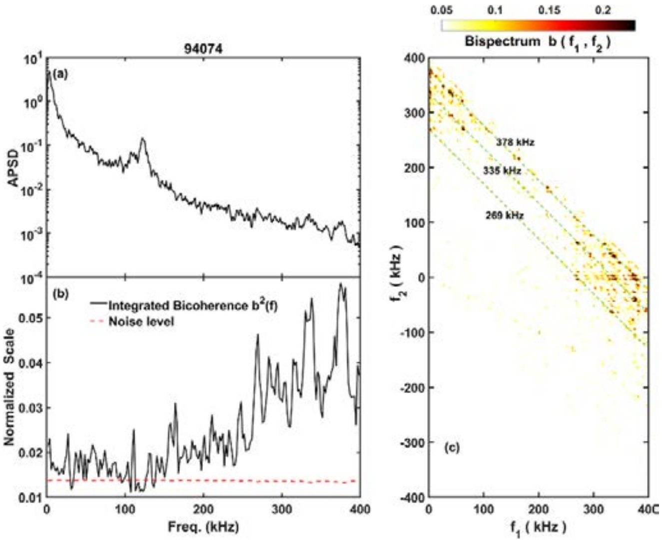

Figure 13. (*a*) APSD of floating potential; (*b*) integrated bicoherence spectrum of floating potential, and the dashed line signifies the noise level; (*c*) bicoherence of floating potential. The floating potential of the probe is located at $R = 2317$ mm in ELM suppression. The green dashed lines in (*c*) denote the trend of turbulence three-wave coupling.

in figure 11(*d*) also reveals a much larger value in the ELM suppression case. The electron density measured by the combined probe is shown in figure 11(*e*), which reveals the same radial structure as the radial turbulent particle and heat flux in figure 11(*c*), i.e. the electron density during ELM suppression is much higher than that in the inter-ELM phase over the whole SOL, demonstrating enhanced particle exhaust in ELM suppression.

To further investigate the contribution of turbulence components on the edge radial turbulent transport in ELM suppression, the fluctuations of the poloidal electric field E_θ in the frequency region of 1–30 kHz, 40–130 kHz and 118–130 kHz are compared with the radial turbulent particle flux Γ_r and divertor particle flux. Since the sampling rate of the RCP is 20 times larger than the DivLP system, the envelopes of the fluctuations δE_θ and turbulent particle flux Γ_r are calculated for comparison. The ion saturation current of a DivLP around the strike point is used to signify the fast temporal evolution of divertor particle flux. The time sequence of the DivLP signal in figure 12(*e*) is shifted by 530 μs backwards, due to the particle transport time along the magnetic field. As illustrated in figures 12(*d*) and (*e*), the peaks of the Γ_r envelope are well consistent with the peaks of divertor particle flux, denoting that the radial particle flux driven by turbulence could increase the divertor particle flux directly during ELM suppression. The envelopes of fluctuations δE_θ in 1–30 kHz, 40–130 kHz and 118–130 kHz are presented in figures 12(*a*)–(*c*), respectively. When there is a peak in the Γ_r envelope, the δE_θ envelopes in both the 1–30 kHz and 40–130 kHz frequency ranges usually peak there, as labeled in the green shaded vertical strips. Furthermore, the fluctuation level of δE_θ in 1–30 kHz is much higher than that in 40–130 kHz, which is consistent with the frequency distribution of turbulent particle flux in figure 11(*b*). Furthermore, the fluctuations δE_θ in 118–130 kHz usually reveal the same peaks as Γ_r, but the corresponding amplitude is much lower than that from 1–30 kHz.

The interaction between different turbulence components has been investigated by performing the bispectral analysis for the floating potential signal [45–48]. The bicoherence $b(f_1,f_2)$ and the integrated bicoherence spectrum $b^2(f)$ are estimated by the following two equations:

$$b(f_1,f_2) = \frac{|\langle X(f_1)X(f_2)X^*(f)\rangle|}{\sqrt{\langle |X(f_1)X(f_2)|^2 |X(f)X^*(f)|\rangle}}, \qquad (4)$$

$$b^2(f) = \sum_{f=f_1\pm f_2} b^2(f_1,f_2), \qquad (5)$$

where $f = f_1 \pm f_2$, the star denotes the complex conjugate, and $X(f)$ is the Fourier component of floating potential $\tilde{\phi}_f$. In figure 13(*a*), during ELM suppression the APSD of floating potential reveals noteworthy peaks at frequencies 5 kHz, 120 kHz, 269 kHz, 320 kHz, 335 kHz and 375 kHz. The integrated bicoherence spectrum in figure 13(*b*) also peaks at these frequency points, and the peaks in high frequency range (>250 kHz) have larger integrated bicoherence. In addition, there are two noteworthy peaks at 27 kHz and 164 kHz in the integrated bicoherence, but the corresponding peaks in the APSD are small. In figure 13(*c*), the $f_2 > 0$ region signifies the sum coupling of $f = f_1 + f_2$, while the $f_2 < 0$ region signifies the difference coupling $f = f_1 - f_2$. Most of the bright structures can be classified into three branches, and each follows the formula $f_1 + f_2 = f_\mathrm{const}$, with $f_\mathrm{const} = 378$ kHz, 335 kHz and 269 kHz for the three dashed lines in figure 13(*c*). These bright structures usually have a low frequency coordinate

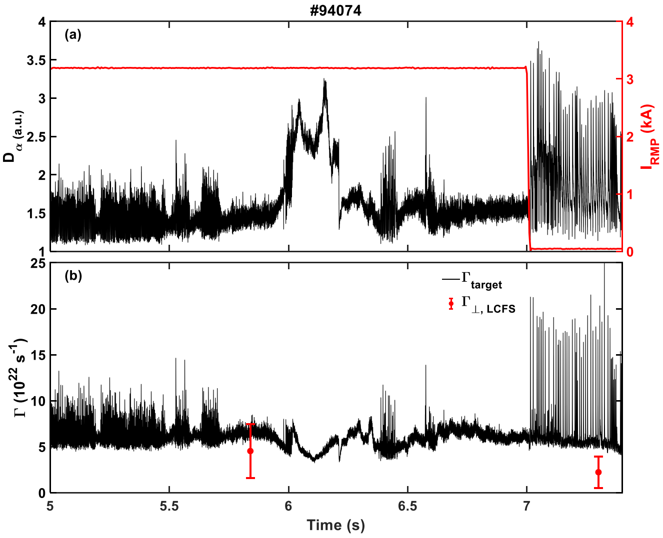

Figure 14. (*a*) D_{α} signal and RMP coil current; (*b*) the total particle deposition on divertor plates (black line) and the radial particle flux across the LCFS measured by the combined probe.

($|f_2| < 60$ kHz when $f_1 > 250$ kHz; or $f_1 < 60$ kHz when $f_2 > 250$ kHz), and the intensity is extremely prominent at the frequency about 5 kHz. There is strong three-wave interaction between the low frequency turbulence and the high frequency turbulence, which could be beneficial to form the low frequency turbulence dominant radial turbulent transport. Note that the three-wave coupling between the 120 kHz electromagnetic mode and other turbulence components is relatively low.

In order to compare the upstream cross-field particle flux with the divertor particle deposition, the cross-field particle flux across the LCFS can be estimated by the equation $\Gamma_{\perp,\mathrm{LCFS}} = \Gamma_{\mathrm{r}} S_{\mathrm{LCFS}}$ with the assumption that the upstream cross-field particle flux is homogenous on the same flux surface, where Γ_{r} is measured at the innermost point of the combined probe and S_{LCFS} is the total area of the LCFS. Note that the radial transport is asymmetric poloidally [49, 50], and the edge transport reveals a strong 3D structure under the application of RMP [51]. Consequently, the total radial particle flux is a rough estimation with some uncertainty. However, with this assumption it is able to directly compare the upstream radial particle transport and the divertor particle deposition, which would be beneficial to the interpretation of edge turbulence transport in ELM suppression with RMP. The total particle flux deposited at divertor is calculated by the sum of particle flux at all the four divertor targets (UI, upper outer, LI, and LO), and the particle flux deposited at one target can be derived from the equation:

$$\Gamma_{\mathrm{t}} = \int_{l_{\mathrm{a}}}^{l_{\mathrm{b}}} \frac{2\pi R_{\mathrm{div}} j_{\mathrm{s}} \left(R_{\mathrm{div}}, l\right) \sin\theta}{e} \mathrm{d}l, \tag{6}$$

where θ is the angle between the magnetic field and the divertor plate plane. As illustrated in figure 14(*b*), the total divertor particle flux during ELM suppression is higher than that in the inter-ELM phase. The estimated upstream total cross-field particle flux is slightly lower than the divertor particle flux during ELM suppression, but the former is half of the latter in the inter-ELM phase. It should be pointed out that the innermost position of Γ_{r} measured by the combined probe is about 3 cm outside the LCFS, where the corresponding turbulent particle flux is smaller than that at the LCFS, which may lead to an underestimation of the total radial particle flux. In addition, the SOL decay length is much shorter in the ELMy plasma [52], which also can be seen in figure 11(*e*), i.e. the electron density in the ELMy phase is much lower in the SOL. This could further undervalue the cross-field particle flux $\Gamma_{\perp,\mathrm{LCFS}}$ in the ELMy phase. Note that the big spike of D_{α} signal within 6–6.2 s in figure 14(*a*) is caused by the deep plunge of RCP, and only the probe data before 5.9 s is used for the analysis in this article. To sum up, it is demonstrated that edge turbulence could play an important role in the upstream radial transport and affect the divertor particle deposition.

5. Discussion

Based on the plasma profiles in figure 3, the growth rate and frequency are simulated by the gyrokinetic solver (CGYRO) for the ELM suppression case [53], as illustrated in figure 15. From the linear growth rate of electromagnetic fluctuations and the electrostatic fluctuations in figure 15(*a*), an electromagnetic mode appears at $\rho = 0.99$ and an electrostatic mode appears at $\rho = 0.98$. From the turbulence frequency in figures 15(*b*) and (*c*), the electromagnetic mode propagates along the ω_{*e} direction with $n = 1$, while the electrostatic mode propagates along the ω_{*i} direction. The electron mode has no clear ballooning structure in the fluctuations of floating potential ϕ and parallel magnetic potential $A_{||}$ from the simulation. Furthermore, this mode almost disappears when $\beta_e \leqslant 0.25\beta_{\mathrm{e,\,exp}}$ in a β_{e} scan, and only a small growth rate variation is observed during the collisionality scan, signifying that the electron mode is sensitive to β_e. The frequency of the electron mode around $\rho = 0.99$ is about 190 kHz. Note that the mode frequency could be changed due to the profile uncertainty and the local $E_{\mathrm{r}} \times B$ shear flow. In consequence, this electron mode satisfies the characteristics of the micro-tearing mode (MTM) [54, 55]. An electrostatic scan with adiabatic electrons is performed to verify the ion mode, which suggests the existence of the ion temperature gradient (ITG) mode [56]. In addition, the frequency of ITG is much lower than that of the MTM in simulation.

In our RMP experiment, the electrostatic mode around 120 kHz has a small $k_{\theta}\rho_{\mathrm{s}} \approx 0.01$–$0.035$, a propagation velocity along the ω_{*e} direction, and a frequency close to the electron diamagnetic drift frequency, which is consistent with the electromagnetic mode in CGYRO simulation. Consequently, the 120 kHz mode is probably the MTM. Recently the MTM has been observed in some tokamaks, such as DIII-D [57], JET [58] and MAST [59], which is believed to drive weak particle transport. In section 4, the 120 kHz mode has a small contribution to the outward particle flux as measured by the

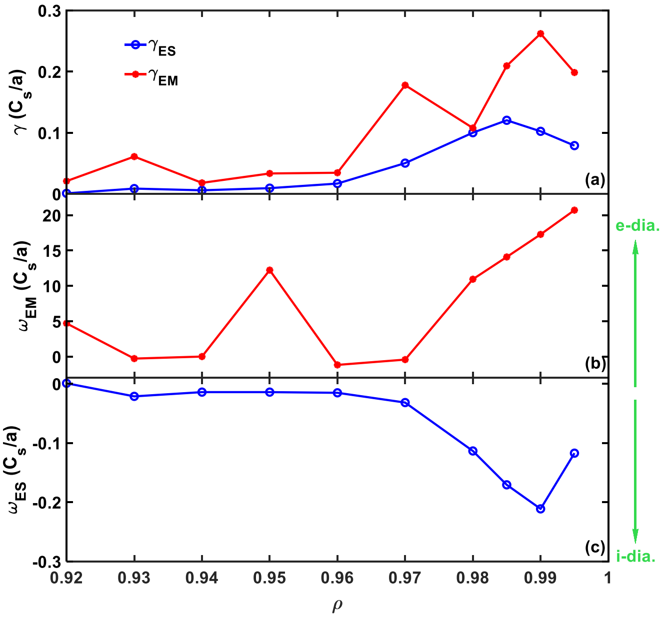

Figure 15. Local simulation results from CGYRO. Growth rate γ (*a*), and frequency ω for the electromagnetic fluctuations (*b*) and the electrostatic fluctuations (*c*). The positive frequency ω is in the electron diamagnetic drift direction, while the negative ω is in the ion diamagnetic drift direction.

combined probe, and the existence of this mode is very weak in the ASPD of the ion saturation current. These experimental results suggest that the 120 kHz mode is the MTM.

The low frequency turbulence below 30 kHz has a $k_\theta \rho_s \approx 0.1$–0.35, a propagation velocity in the ω_{*i} direction, and a frequency much smaller than the ion diamagnetic drift frequency, which agrees with the ITG turbulence in the CGYRO simulation. Usually, the ITG turbulence could drive significant radial particle transport [2], which is consistent with the measurement in the ELM suppression case.

6. Conclusion

The edge turbulence characteristics and the induced radial transport have been investigated in the ELM suppression experiments with $n = 4$ RMP coils on EAST. With the increase of plasma current I_p and the decrease of q_{95}, ELM suppression is achieved when $q_{95} \approx 3.6$ and $\nu_e^* \approx 0.5$, which are close to the ITER plasma conditions. During ELM suppression, clear density pump-out is observed in the core plasma, but the plasma stored energy is almost constant. During ELM suppression, the electron density increases about two times over a wide radial region in the SOL. The edge turbulence below 200 kHz measured by the PCR is significantly enhanced during ELM suppression, compared with the inter-ELM phase. In this experiment, the SOL turbulence structure is measured by a dedicated combined probe. In contrast with the turbulence in the inter-ELM phase without RMP, the low frequency turbulence (<30 kHz) rises significantly in the near SOL during ELM suppression. In this low frequency, two coherent modes at 5 kHz and 27 kHz are clear in the Mirnov coil and floating potential during ELM suppression. Furthermore, an electromagnetic mode around 120 kHz with a toroidal mode number $n = 1$ is observed by the Mirnov coil and the combined probe in ELM suppression, and it is absent in ELM mitigation and the natural ELMy phase. This electromagnetic mode can be detected from $R = 2330$ mm (about 45 mm away from the LCFS with $R_{\mathrm{LCFS}} = 2285$ mm) and becomes more prominent in the near SOL, with $k_\theta = 0.15$ cm^{-1} along the electron diamagnetic drift (ω_{*e}) direction. As derived from the two-point cross-correlation analysis, the low frequency turbulence (<30 kHz) in the near SOL propagates in the ion diamagnetic drift (ω_{*i}) direction with a velocity of 0.35 km s^{-1} in the plasma frame; the broadband turbulence between 40–120 kHz propagates in the ω_{*e} direction with a velocity of 3.4 km s^{-1} in the plasma frame. In the near SOL, the poloidal correlation length of turbulence within 1–400 kHz is 1.5–2.5 cm, and the turbulence phase velocity increases sharply in the ω_{*e} direction. A set of CGYRO simulations are performed to illustrate the nature of the 120 kHz mode and the low frequency turbulence, suggesting that the former is the MTM and the latter is the ITG mode.

The radial turbulent particle flux Γ_r is calculated from the combined probe measurement in both the time and frequency domains. Compared with the inter-ELM phase, the turbulent particle flux during ELM suppression can be five times larger in the near SOL, which is consistent with the higher electron density in the whole SOL. The radial turbulent particle flux is mainly driven by the low frequency turbulence below 30 kHz. The 120 kHz electromagnetic mode also contributes to outward particle flux, which is much lower than the low frequency turbulence. A comparison is performed between the upstream radial turbulent particle flux and the divertor particle flux near the strike point, and both particle fluxes reveal the same temporal evolution when the divertor particle flux is shifted by a parallel transport time delay (about 500 μs) in the SOL, demonstrating that the upstream turbulent particle flux could increase the divertor particle deposition directly. The fluctuations δE_θ in the low frequency region (1–30 kHz) and the broadband turbulence region (40–130 kHz) exhibit the same peaks as the radial turbulent particle flux in the time sequence. But the fluctuation level of the low frequency turbulence is much larger than the broadband turbulence, which is consistent with the frequency distribution of radial turbulent particle flux. The bispectral analysis is performed to obtain the three-wave coupling of turbulence. There is strong three-wave interaction between the low frequency and high frequency (>250 kHz) turbulence, which could be beneficial to form the low frequency turbulence dominant radial turbulent transport. Under the assumption that the cross-field turbulent particle flux is homogeneous on the same flux surface, the upstream radial particle flux measured by the combined probe is consistent with the total particle flux deposited on the divertor targets during the ELM suppression, indicating that the edge turbulence plays an important role in the radial transport and divertor particle deposition under the application of $n = 4$ RMP.

In summary, the edge turbulence and the induced radial particle flux are enhanced significantly during the ELM suppression by using $n = 4$ RMP. The low frequency turbulence below 30 kHz dominates the turbulent particle flux in ELM suppression, and the three-wave coupling between the low frequency and high frequency turbulence could be probably contribute to the radial transport. The electromagnetic mode around 120 kHz also contributes to outward particle flux, but it is relatively low compared to the low frequency turbulence. The enhanced radial turbulent particle transport is an important mechanism for the particle exhaust, which helps to maintain the ELM suppression with a lower pedestal electron density and pressure than the inter-ELM phase. The contributions of electromagnetic and electrostatic fluctuations to the radial transport will be analyzed in the future.

Acknowledgments

This work was supported by the National MCF Energy R&D Program of China (Nos. 2022YFE03020004, 2022YFE03030001, 2019YFE03040000, 2019YFE03030000, 2017YFE0301100 and 2022YFE03050003), the National Natural Science Foundation of China (Nos. 11875294, 12275310, 12075281, 12175277 and 11975271), the Science Foundation of Institute of Plasma Physics, Chinese Academy of Sciences, No. DSJJ-2021-01, the Collaborative Innovation Program of Hefei Science Center, CAS, No. 2021HSC-CIP019, and the Users with Excellence Program of Hefei Science Center, CAS under grant Nos. 2021HSC-UE014 and 2021HSC-UE012.

ORCID iDs

S.C. Liu https://orcid.org/0000-0002-7298-0680
T.F. Tang https://orcid.org/0000-0002-8698-9985
N. Yan https://orcid.org/0000-0002-2536-5853
T.H. Shi https://orcid.org/0000-0002-5321-1464
K.X. Ye https://orcid.org/0000-0003-0927-4502
L.Y. Meng https://orcid.org/0000-0002-8633-5383
R. Ding https://orcid.org/0000-0003-2880-9736
Y. Sun https://orcid.org/0000-0002-9934-1328
M. Jia https://orcid.org/0000-0002-1672-9782
Q. Ma https://orcid.org/0000-0001-8057-8934
J.L. Wei https://orcid.org/0000-0002-2371-3842
T. Zhang https://orcid.org/0000-0002-1555-6226
Y.F. Jin https://orcid.org/0000-0002-3061-6709
W.Y. Wei https://orcid.org/0000-0003-3072-4520
X. Han https://orcid.org/0000-0002-6255-3220
L. Wang https://orcid.org/0000-0002-8373-117X
L. Zeng https://orcid.org/0000-0003-4968-1401
G.S. Xu https://orcid.org/0000-0001-8495-8678
X. Gao https://orcid.org/0000-0003-1885-2538

References

[1] Hill D.N. 1997 *J. Nucl. Mater.* **241–243** 182
[2] Doyle E.J. *et al* 2007 *Nucl. Fusion* **47** S18
[3] Eich T., Sieglin B., Scarabosio A., Fundamenski W., Goldston R.J. and Herrmann A. 2011 *Phys. Rev. Lett.* **107** 215001
[4] Burrell K.H. *et al* 2005 *Plasma Phys. Control. Fusion* **47** B37
[5] Liang Y. *et al* 2009 *J. Nucl. Mater.* **390–391** 733
[6] Liang Y., Gimblett C.G., Browning P.K., Devoy P., Koslowski H.R., Jachmich S., Sun Y. and Wiegmann C. 2010 *Phys. Rev. Lett.* **105** 065001
[7] Suttrop W. *et al* 2011 *Phys. Rev. Lett.* **106** 225004
[8] Kirk A., Liu Y., Nardon E., Tamain P., Cahyna P., Chapman I., Denner P., Meyer H., Mordijck S. and Temple D. 2011 *Plasma Phys. Control. Fusion* **53** 065011
[9] Sun Y. *et al* 2016 *Phys. Rev. Lett.* **117** 115001
[10] Kim J. *et al* 2012 *Nucl. Fusion* **52** 114011
[11] Sun T.F., Liu Y., Ji X.Q., Liu Y.Q., Ke R., Gao J.M., Wu N., Deng W., Xu M. and Duan X.R. 2021 *Nucl. Fusion* **61** 036020
[12] Evans T.E. 2015 *Plasma Phys. Control. Fusion* **57** 123001
[13] Kirk A. *et al* 2013 *Plasma Phys. Control. Fusion* **55** 124003
[14] Evans T.E. *et al* 2008 *Nucl. Fusion* **48** 024002
[15] Jia M. *et al* 2018 *Nucl. Fusion* **58** 046015
[16] Schmitz O. *et al* 2013 *J. Nucl. Mater.* **438** S194
[17] Liu Y.Q., Ham C.J., Kirk A., Li L., Loarte A., Ryan D.A., Sun Y., Suttrop W., Yang X. and Zhou L. 2016 *Plasma Phys. Control. Fusion* **58** 114005
[18] Li L., Liu Y.Q., Loarte A., Pinches S.D., Polevoi A., Becoulet M., Huijsmans G.T.A. and Zhong F.C. 2022 *Nucl. Fusion* **62** 096008
[19] Orain F. *et al* 2013 *Phys. Plasmas* **20** 102510
[20] McKee G.R. *et al* 2013 *Nucl. Fusion* **53** 113011
[21] Taimourzadeh S., Shi L., Lin Z., Nazikian R., Holod I. and Spong D. 2019 *Nucl. Fusion* **59** 046005
[22] Leuthold N. 2020 Experimental investigation of enhanced particle transport due to magnetic perturbations on ASDEX upgrade *PhD Thesis* Ludwig-Maximilians-Universitaet Muenchen
[23] Lee J., Jeon Y.M., In Y., Park G.Y., Yun G.S., Lee W., Kim M., Lee J.H., Ko W.H. and Park H.K. 2019 *Nucl. Fusion* **59** 066033
[24] Liu S.C. *et al* 2020 *Nucl. Fusion* **60** 082001
[25] Sun Y., Liang Y., Qian J., Shen B. and Wan B. 2015 *Plasma Phys. Control. Fusion* **57** 045003
[26] Sun Y. *et al* 2017 *Nucl. Fusion* **57** 036007
[27] Sun Y. *et al* 2021 *Nucl. Fusion* **61** 106037
[28] Jia M.N. *et al* 2021 *Nucl. Fusion* **61** 106023
[29] Wan B.N. *et al* 2019 *Nucl. Fusion* **59** 112003
[30] Yao D.M. *et al* 2015 *Fusion Eng. Des.* **98–99** 1692
[31] Zhang W. *et al* 2010 *Rev. Sci. Instrum.* **81** 113501
[32] Ming T.F., Zhang W., Chang J., Wang J., Xu G., Ding S., Yan N., Gao X. and Guo H. 2009 *Fusion Eng. Des.* **84** 57
[33] Xu J.C. *et al* 2016 *Rev. Sci. Instrum.* **87** 083504
[34] Xiang H.M. *et al* 2018 *Rev. Sci. Instrum.* **89** 10H103
[35] Liu H.Q. *et al* 2016 *Rev. Sci. Instrum.* **87** 11D903
[36] Wang Y.M. *et al* 2019 *Fusion Eng. Des.* **148** 111286
[37] Zang Q., Junyu Z., Li Y., Qingsheng H., Yanqing J., Tao Z., Xiaoqi X., Bhatti S.H. and Xiang G. 2010 *Plasma Sci. Technol.* **12** 144
[38] Sauter O., Angioni C. and Lin-Liu Y.R. 1999 *Phys. Plasmas* **6** 2834
[39] Shi T.H. *et al* 2013 *Plasma Phys. Control. Fusion* **55** 055007
[40] Chen R. *et al* 2018 *Nucl. Fusion* **58** 112004
[41] Ye Y. *et al* 2021 *Nucl. Fusion* **61** 126050
[42] Zhao J.Q., Sun Y., Chu N., Shi T., Ma Q., Wang Y., He K. and Hu Y. 2021 *Plasma Sci. Technol.* **23** 095101
[43] Beall J.M., Kim Y.C. and Powers E.J. 1982 *J. Appl. Phys.* **53** 3933
[44] Levinson S.J., Beall J.M., Powers E.J. and Bengtson R.D. 1984 *Nucl. Fusion* **24** 527
[45] Nagashima Y. *et al* 2007 *Plasma Phys. Control. Fusion* **49** 1611

[46] Hidalgo C., Sánchez E., Estrada T., Brañas B., Ritz C.P., Uckan T., Harris J. and Wootton A.J. 1993 *Phys. Rev. Lett.* **71** 3127

[47] Diamond P.H., Rosenbluth M.N., Sanchez E., Hidalgo C., Van Milligen B., Estrada T., Brañas B., Hirsch M., Hartfuss H.J. and Carreras B.A. 2000 *Phys. Rev. Lett.* **84** 4842

[48] Wang H.Q. *et al* 2014 *Nucl. Fusion* **54** 124001

[49] Zhang D.R., Chen Y.P., Xu X.Q., Xia T.Y. and Liu S.C. 2020 *Nucl. Fusion* **60** 106015

[50] Zeiler A., Biskamp D., Drake J.F. and Rogers B.N. 1998 *Phys. Plasmas* **5** 2654

[51] Thornton A.J., Kirk A., Cahyna P., Chapman I.T., Harrison J.R. and Liu Y. 2014 *Nucl. Fusion* **54** 14

[52] Brida D., Lunt T., Faitsch M., Wischmeier M., Feng Y., Suttrop W., Stroth U. and Eich T. 2019 *Nucl. Mater. Energy* **19** 205

[53] Candy J., Belli E.A. and Bravenec R.V. 2016 *J. Comput. Phys.* **324** 73

[54] Doerk H., Jenko F., Görler T., Told D., Pueschel M.J. and Hatch D.R. 2012 *Phys. Plasmas* **19** 055907

[55] Kotschenreuther M. *et al* 2019 *Nucl. Fusion* **59** 096001

[56] Horton W., Lindberg D., Kim J.Y., Dong J.Q., Hammett G.W., Scott S.D., Zarnstorff M.C. and Hamaguchi S. 1992 *Phys. Fluids* B **4** 953

[57] Hassan E., Hatch D.R., Halfmoon M.R., Curie M., Kotchenreuther M.T., Mahajan S.M., Merlo G., Groebner R.J., Nelson A.O. and Diallo A. 2022 *Nucl. Fusion* **62** 026008

[58] Hatch D.R. *et al* 2021 *Nucl. Fusion* **61** 036015

[59] Hillesheim J.C., Dickinson D., Roach C.M., Saarelma S., Scannell R., Kirk A., Crocker N.A., Peebles W.A. and Meyer H. 2016 *Plasma Phys. Control. Fusion* **58** 014020